doi:10.1038/nature16168

Weakened magnetic braking as the origin of anomalously rapid rotation in old field stars

Jennifer L. van Saders[1,2,3], Tugdual Ceillier[4], Travis S. Metcalfe[5], Victor Silva Aguirre[6], Marc H. Pinsonneault[3,7], Rafael A. García[3,4], Savita Mathur[3,5] & Guy R. Davies[6,8]

A knowledge of stellar ages is crucial for our understanding of many astrophysical phenomena, and yet ages can be difficult to determine. As they become older, stars lose mass and angular momentum, resulting in an observed slowdown in surface rotation[1]. The technique of 'gyrochronology' uses the rotation period of a star to calculate its age[2,3]. However, stars of known age must be used for calibration, and, until recently, the approach was untested for old stars (older than 1 gigayear, Gyr). Rotation periods are now known for stars in an open cluster of intermediate age[4] (NGC 6819; 2.5 Gyr old), and for old field stars whose ages have been determined with asteroseismology[5,6]. The data for the cluster agree with previous period–age relations[4], but these relations fail to describe the asteroseismic sample[7]. Here we report stellar evolutionary modelling[5,6,8–10], and confirm the presence of unexpectedly rapid rotation in stars that are more evolved than the Sun. We demonstrate that models that incorporate dramatically weakened magnetic braking for old stars can—unlike existing models—reproduce both the asteroseismic and the cluster data. Our findings might suggest a fundamental change in the nature of ageing stellar dynamos, with the Sun being close to the critical transition to much weaker magnetized winds. This weakened braking limits the diagnostic power of gyrochronology for those stars that are more than halfway through their main-sequence lifetimes.

There are two approaches to the calibration and testing of gyrochronology. The first is a purely empirical approach, which uses a sample of stars with independently measured ages and rotation periods to construct period–age relationships. These relationships are generally simple power laws that take into account age, period, and some mass-dependent quantity; they have seen wide usage[1,2,4,5,7]. The second, model-based approach uses stellar models and a prescription for magnetic braking to account for the functional dependence of the rotation period on all relevant stellar quantities, but relies on calibrators to determine the magnitude of the angular momentum loss. For this reason, the model-based approach is well suited to calibrating samples that cover parameter space only sparsely; it also provides a method for attaching physical meaning to observed braking behaviour.

Magnetic-braking prescriptions are typically scaled from the solar case; for example, the Skumanich relation[1] yields angular momentum loss of the form $dJ/dt \propto \omega^3$, where t is time, J is angular momentum, and ω is the angular rotation velocity[11]. These relations often use the dimensionless Rossby number—defined as the ratio of the rotation period to the convective overturn timescale, $Ro = P/\tau_{cz}$—to characterize departures from this simple power law. Rossby-number thresholds and scalings are routinely invoked to parameterize the magnetic-field strength[12,13]; the dependence of the spin-down on stellar mass and composition[2,14]; the observed saturation of magnetic braking in rapid rotators; and the sharp transition from slow to rapid rotation that occurs in hot stars (of greater than 6,250 K) because of their thinning convective envelopes[14]. Under traditional prescriptions, stars undergo braking throughout their main-sequence lifetimes, regardless of rotation rate. Observations of stellar clusters of young and intermediate ages have indicated that such treatments are reasonable[4,15]. However, there is a dearth of old stars with which to test such relationships, owing to the long-period, low-amplitude signatures of rotation in such stars, and to the challenge of age measurements in field stars. Data from the Kepler telescope provide a first test of these prescriptions in stars that are older than the Sun.

The high-precision, long-baseline light curves from Kepler make such investigations possible. The rotation of a star manifests itself in Kepler data as a periodic modulation in the intensity, as dark starspots rotate into and out of view. Intensity variations due to stellar oscillations are likewise present in the light curve, on shorter timescales. Low-degree modes of oscillation probe the conditions of the deep stellar interior and internal structure of the star, providing ages that are precise to better than 10% in stars for which many oscillation modes are detected at high signal-to-noise ratios[16].

The first efforts to calibrate the gyrochronology relations using Kepler seismic targets uncovered tension between the cluster and seismic samples[7]. Although the form of the mass–period–age relation used in this study[7] was similar to those in previous studies[2,4], the range of ages and more sophisticated treatment of observational uncertainties made it possible to determine that the sample did not obey a single power-law period–age relation. However, even this approach has limitations: it does not account for metallicity or for changes in the stellar moment of inertia, and it relied on a sample for which detailed seismic modelling and spectroscopic data were lacking for some stars, biasing the seismic ages.

To address the limitations of previous work and to take full advantage of precisely determined stellar parameters, we utilize a subset of 21 Kepler stars—selected to have detailed asteroseismic modelling and high-precision ages, measured rotation periods, and measured metallicities[5,6,8–10]—and couple these observations to stellar evolutionary models. Sample selection, details of the modelling to derive asteroseismic ages, and extraction of rotation periods are described in the Methods. Figure 1 shows the surface—in terms of period, age and effective temperature (T_{eff}, a proxy for mass)—upon which the stars are expected to lie[2,4]. Actual cluster and seismic data are overplotted; while the clusters and young asteroseismic targets lie close to the plane, the intermediate-age and old asteroseismic stars are strikingly discrepant and nearly all lie below the surface, owing to the fact that they are rotating more rapidly than expected. When we account

[1]Carnegie Observatories, 813 Santa Barbara Street, Pasadena, California 91101, USA. [2]Department of Astrophysical Sciences, Princeton University, Princeton, New Jersey 08544, USA. [3]Kavli Institute for Theoretical Physics, University of California, Santa Barbara, California 93106-4030, USA. [4]Laboratoire AIM, Alternative Energies and Atomic Energy Commission (CEA)/Physical Sciences Division (DSM)–Centre National d'Études Spatiales (CNRS)–Université Paris Diderot–Institute of Research into the Fundamental Laws of the Universe (IRFU)/Service d'Astrophysique (SAp), Centre de Saclay, 91191 Gif-sur-Yvette Cedex, France. [5]Space Science Institute, 4750 Walnut Street Suite 205, Boulder, Colorado 80301, USA. [6]Stellar Astrophysics Centre, Department of Physics and Astronomy, Aarhus University, Ny Munkegade 120, DK-8000 Aarhus, Denmark. [7]Ohio State University, Department of Astronomy, 140 West 18th Avenue, Columbus, Ohio 43210, USA. [8]School of Physics and Astronomy, University of Birmingham, Birmingham B15 2TT, UK.

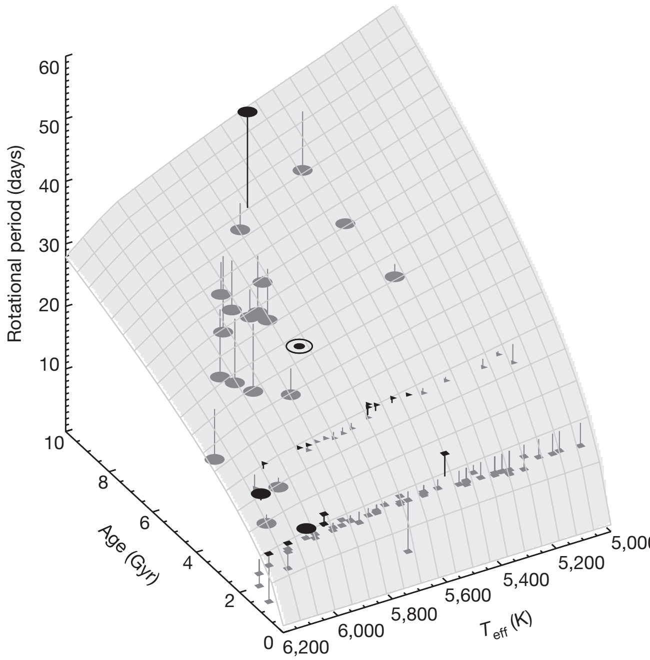

Figure 1 | The period–age plane as predicted by gyrochronology, compared with observed periods. The empirical gyrochronology relation[2,4] is shown as a plane. Data from open stellar clusters are shown as small squares (NGC 6811 cluster; 1 Gyr) and triangles (NGC 6819 cluster; 2.5 Gyr). Large circles represent the seismic sample of 21 stars that are detected in the Kepler data; this sample falls systematically below the plane. The solar symbol (⊙) marks the Sun, which falls on the plane by design. The effective temperature, T_{eff}, is a proxy for mass.

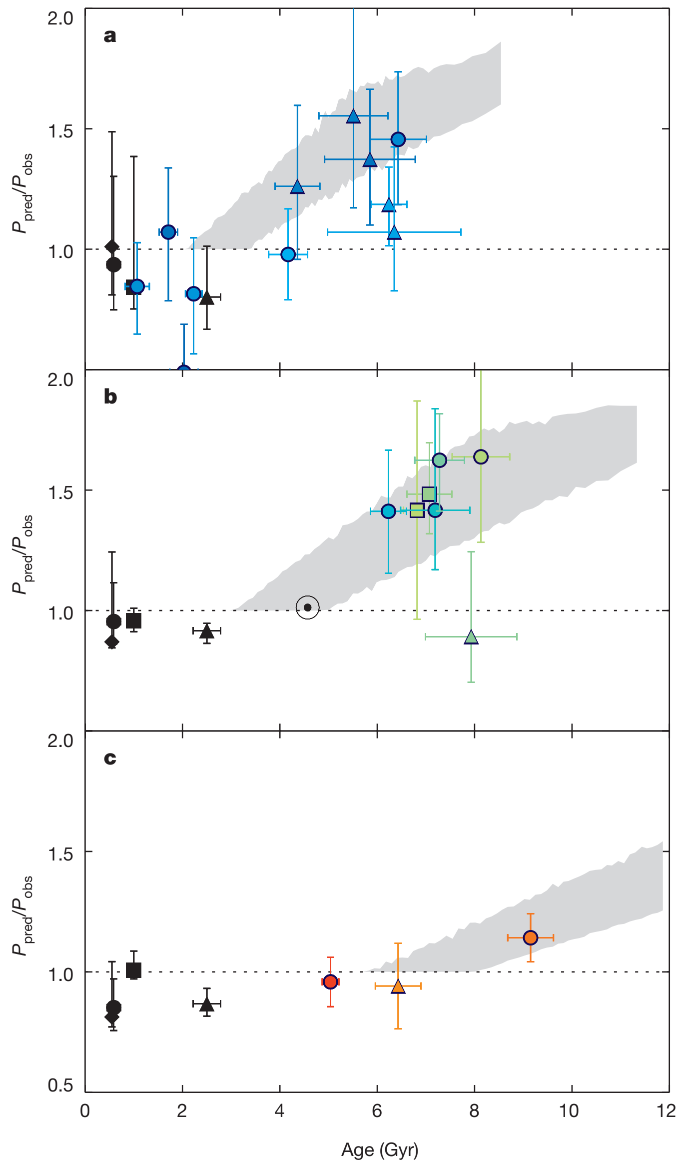

Figure 2 | Ratios of the predicted rotation period[14] to the observed period. Predicted rotation periods are derived from existing period–age relations; observed periods are as detected by the Kepler telescope. These ratios are plotted against stellar age. Stars are divided according to decreasing ZAMS T_{eff}: **a**, 5,900–6,200 K; **b**, 5,600–5,900 K; **c**, 5,100–5,400 K. Period ratios for open clusters are shown as black symbols, as follows: diamonds, M37; circles, Praesepe; squares, NGC 6811; triangles, NGC 6819. The Sun (⊙) is also marked. Coloured circles represent seismic targets; coloured triangles represent known planet hosts; coloured squares represent the binary stars 16 Cygni A and B. All errors are shown to 1σ. Stars are coloured according to ZAMS T_{eff}, with blue representing the hottest stars and red the coolest stars. Shaded regions represent the period ratios permitted in each T_{eff} bin for a model in which $Ro_{crit} = 2.16$.

for uncertainties in the ages, masses, and compositions (see Methods) and predict the rotation periods that we should have observed given existing period–age relations[2,14] ($P_{expected}$), we find that the systematic offset persists; stars of roughly solar age and older are rotating more rapidly than predicted, regardless of the chosen period–age relation. Figure 2 highlights the systematic offset by plotting the ratios of the expected to observed periods for each star in the sample, where the expected periods are calculated using stellar models with a braking law calibrated on the Sun and on open clusters[14] (a similar plot is provided in Extended Data Fig. 3 for the empirical relation[2]). The theoretical models[14] fit the data with a χ^2 value of 54.9, whereas the empirical relation[2] yields a χ^2 of 155.6. In both cases, the systematic offset towards short rotation periods is an indication that the models predict more angular momentum loss than actually occurs.

We therefore conclude that magnetic braking is weaker in these intermediate-age and old stars. We extend our model by postulating that, in addition to the Rossby scaling already present in the theoretical models[14], effective loss of angular momentum ceases above a critical Rossby threshold[12]. We modify the prescription for angular momentum loss[14] to conserve angular momentum above a specified Ro_{crit}. Graphs showing the effects of varying Ro_{crit} values on the models are provided in Fig. 3. The inclusion of the threshold has the desired effect: it reproduces the existing gyrochronology relations and cluster data at young ages, when Ro is smaller because of more rapid rotation, but allows stars to maintain unusually rapid rotation periods at late times. Furthermore, it reproduces the trend in mass that is apparent in Figs 2 and 3 (and the trend in the zero-age main-sequence (ZAMS) T_{eff}, which selects stars with similar rotational histories; we perform all fits using the seismic mass, but use ZAMS T_{eff} for display to simplify the figures). Hotter, more massive stars reach the critical Rossby threshold at younger ages, and we therefore see discrepancies between the fiducial gyrochronology relationships and the observations at earlier times as ZAMS T_{eff} increases. The best-fit value for the Rossby threshold, given our sample, is $Ro_{crit} = 2.16 \pm 0.09$ ($\chi^2 = 13.3$) for the modified models. The shaded grey regions in Figs 2 and 3 denote the full range of period ratios ($P_{Rocrit}/P_{fiducial}$), and the period–age combinations allowed for a model with $Ro_{crit} = 2.16$, given the ranges of ZAMS T_{eff} that are represented in each panel. These regions encompass all combinations of mass (0.4–2.0 solar masses) and metallicity ($-0.4 < [Z/H] < +0.4$) that together produce a star within the appropriate ZAMS T_{eff} range for each panel of Figs 2 and 3, on both the main-sequence and the subgiant branch.

We emphasize that our result—that old stars are rotating anomalously rapidly—persists regardless of the choice of period–age

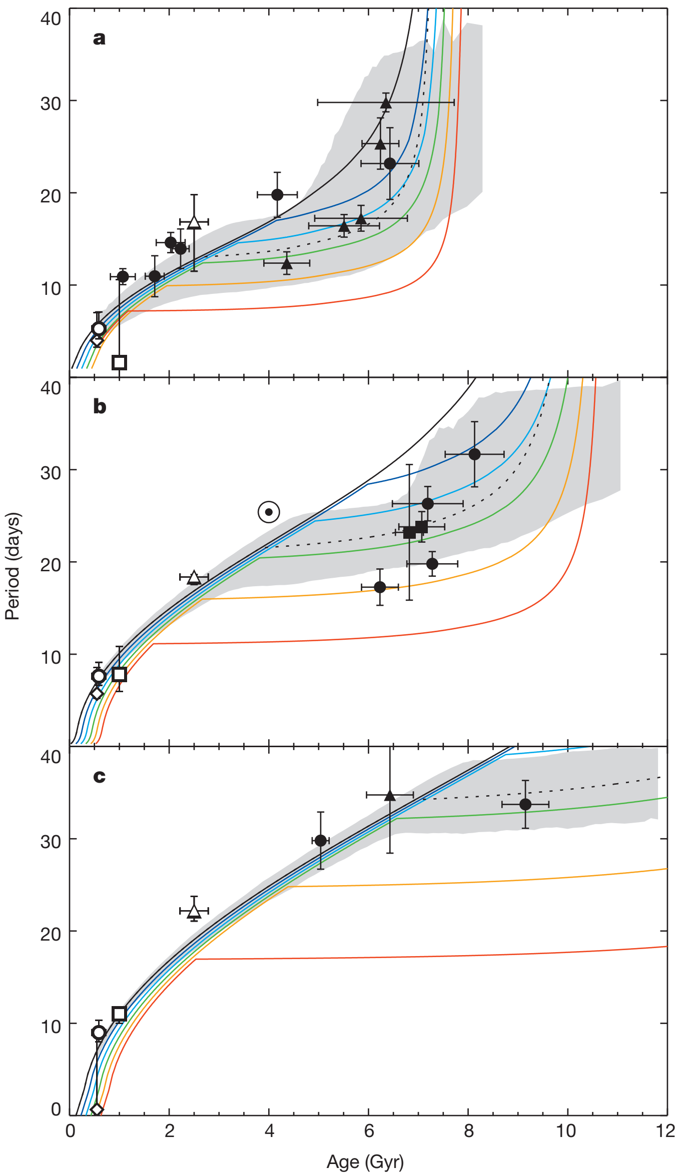

Figure 3 | The effects of a Ro_{crit} threshold on rotational evolution. Panels are divided according to decreasing ZAMS T_{eff}: **a**, 5,900–6,200 K; **b**, 5,600–5,900 K; **c**, 5,100–5,400 K (as in Fig. 2). Black symbols represent open stellar clusters, as follows: diamonds, M37; circles, Praesepe; squares, NGC 6811; triangles, NGC 6819. The Sun (⊙) is also marked. Model curves are shown for solar metallicity and ZAMS T_{eff} 6,050 K (**a**), 5,750 K (**b**), and 5,250 K (**c**). Curves are colour-coded by Ro_{crit}: black, no Ro_{crit} cut; dark blue, $Ro_{crit} = 1.0$; light blue, $Ro_{crit} = 1.5$; green, $Ro_{crit} = 2.0$; orange, $Ro_{crit} = 2.5$; red, $Ro_{crit} = 3.0$; dashed black, $Ro_{crit} = 2.16$. Successive curves are offset by +0.1 Gyrs to improve readability. Seismic (cluster) targets are overplotted in solid (open) symbols with 1σ errors. Shaded regions represent $Ro_{crit} = 2.16$ models for each T_{eff} range.

relationship, asteroseismic modelling pipeline, or model uncertainties from the literature (see Methods). The period-detection algorithms[17] and seismic ages have been well tested[8]. The tight rotational sequences observed in intermediate-age open clusters[4] suggest that we are not simply detecting the rapidly rotating tail of a population with a wide distribution of rotation rates, and it is unlikely that our 21 stars with detected rotation rates are atypical (see Methods for further discussion).

Our model represents the limiting case in which the braking is so ineffective that the star ceases to shed angular momentum. If we instead allow the exponent, α, of the period–age relation $P \propto t^{1/\alpha}$ to vary, while fixing Ro_{crit} to the solar Ro value of 2.16, we do not obtain a comparable fit in the old stars until α is greater than ~20, suggesting that the braking is indeed drastically reduced. However, we do observe spot modulation in these stars, which implies at least small-scale magnetic activity. The starspot properties may or may not directly reflect changes in the large-scale magnetic field that governs spin-down. A change in field geometry from a simple dipole to higher-order fields could produce weakened braking[18,19], as could a change in the distribution of spots on the stellar surface[20]. It could also be the case that the large-scale field strength undergoes a transition at high Rossby numbers[12]. Abrupt changes in the efficiency of angular momentum loss have been proposed in order to explain the rotational distributions in young clusters[21], and there is evidence for a Rossby-number-governed shift in field morphologies in low-mass M dwarfs[22]. Observations of detailed magnetic-field morphologies and corresponding simulations are lacking for stars at higher Rossby numbers than the Sun, and both are critical to understanding the source of the observed anomalous rotation.

Regardless of the mechanism that governs the spin-down, the observation that existing rotation–age relationships do not predict the observed rotation rates has immediate implications for gyrochronology. The rotation periods of the middle-aged stars that have passed this Rossby threshold represent only lower limits on the age. The empirical calibrations must be modified, and the weakened relationship between period and age will result in substantially more uncertain rotation-based ages for stars in the latter halves of their lives. The presence of such a Rossby threshold defines boundaries in mass–age space, past which gyrochronology is incapable of delivering precise ages.

Online Content Methods, along with any additional Extended Data display items and Source Data, are available in the online version of the paper; references unique to these sections appear only in the online paper.

Received 3 June; accepted 15 October 2015.
Published online 4 January; corrected online 13 January 2016 (see full-text HTML version for details).

1. Skumanich, A. Time scales for CA II emission decay, rotational braking, and lithium depletion. *Astrophys. J.* **171,** 565–567 (1972).
2. Barnes, S. A. A simple nonlinear model for the rotation of main-sequence cool stars. I. Introduction, implications for gyrochronology, and color-period diagrams. *Astrophys. J.* **722,** 222–234 (2010).
3. Epstein, C. R. & Pinsonneault, M. H. How good a clock is rotation? The stellar rotation-mass-age relationship for old field stars. *Astrophys. J.* **780,** 159–183 (2014).
4. Meibom, S. *et al.* A spin-down clock for cool stars from observations of the 2.5-billion-year-old cluster. *Nature* **517,** 589–591 (2015).
5. García, R. A. Rotation and magnetism of *Kepler* pulsating solar-like stars. Towards asteroseismically calibrated age-rotation relations. *Astron. Astrophys.* **572,** A34–A49 (2014).
6. Ceillier, T. *et al.* Rotation periods and seismic ages of KOIs—comparison with stars without detected planets from *Kepler* observations. *Mon. Not. R. Astron. Soc.* **456,** 119–125 (2016).
7. Angus, R. & Aigrain, S., Foreman-Mackey, D. & McQuillan, A. Calibrating gyrochronology using *Kepler* asteroseismic targets. *Mon. Not. R. Astron. Soc.* **450,** 1787–1798 (2015).
8. Mathur, S. *et al.* A uniform asteroseismic analysis of 22 solar-type stars observed by *Kepler*. *Astrophys. J.* **749,** 152 (2012).
9. Metcalfe, T. S. *et al.* Properties of 42 solar-type *Kepler* targets from the asteroseismic modeling portal. *Astrophys. J.* **214** (Suppl.), 27–40 (2014).
10. Silva Aguirre, V. Ages and fundamental properties of *Kepler* exoplanet host stars from asteroseismology. *Mon. Not. R. Astron. Soc.* **452,** 2127–2148 (2015).
11. Kawaler, S. D. Angular momentum loss in low-mass stars. *Astrophys. J.* **333,** 236–247 (1988).
12. Durney, B. R. & Latour, J. On the angular momentum loss of late-type stars. *Geophys. Astrophys. Fluid Dyn.* **9,** 241–255 (1977).
13. Noyes, R. W., Hartmann, L. W., Baliunas, S. L., Duncan, D. K. & Vaughan, A. H. Rotation, convection, and magnetic activity in lower main-sequence stars. *Astrophys. J.* **279,** 763–777 (1984).
14. van Saders, J. L. & Pinsonneault, M. H. Fast star, slow Star; old Star, young Star: subgiant rotation as a population and stellar physics diagnostic. *Astrophys. J.* **776,** 67–87 (2013).
15. Hartman, J. D. *et al.* Deep MMT transit survey of the open cluster M37. III. Stellar rotation at 550 Myr. *Astrophys. J.* **691,** 342–364 (2009).
16. Metcalfe, T. S. *et al.* Asteroseismology of the solar analogs 16 Cyg A and B from *Kepler* observations. *Astrophys. J.* **748,** L10–L16 (2012).
17. Aigrain, S. *et al.* Testing the recovery of stellar rotation signals from *Kepler* light curves using a blind hare-and-hounds exercise. *Mon. Not. R. Astron. Soc.* **450,** 3211–3226 (2015).

18. Réville, V., Brun, A. S., Matt, S. P., Strugarek, A. & Pinto, R. F. The effect of magnetic topology on thermally driven wind: toward a general formulation of the braking law. *Astrophys. J.* **798,** 116–131 (2015).
19. Garraffo, C., Drake, J. J. & Cohen, O. The dependence of stellar mass and angular momentum losses on latitude and on active region and dipolar magnetic fields. *Astrophys. J.* **807,** L6 (2015).
20. Cohen, O., Drake, J. J., Kashyap, V. L. & Gombosi, T. I. The effect of magnetic spots on stellar winds and angular momentum loss. *Astrophys. J.* **699,** 1501–1510 (2009).
21. Brown, T. The metastable dynamo model of stellar rotational evolution. *Astrophys. J.* **789,** 101–113 (2014).
22. Morin, J., Dormy, E., Schrinner, M. & Donati, J.-F. Weak- and strong-field dynamos: from the Earth to the stars. *Mon. Not. R. Astron. Soc.* **418,** L133–L137 (2011).

Acknowledgements We wish to thank the Kavli Institute for Theoretical Physics and the organizers of the 'Galactic Archaeology and Precision Stellar Astrophysics' program held from January to April 2015. We thank B. Shappee for useful discussions. J.L.v.S. is a Carnegie-Princeton Fellow. T.S.M acknowledges the adopt-a-star crowdfunding program administered by White Dwarf Research Corp. G.R.D. acknowledges the support of the UK Science and Technology Facilities Council (STFC). M.H.P, T.S.M. and S.M. acknowledge support from NASA grant NNX15AF13G and National Science Foundation (NSF) grant AST-1411685. T.C. and R.A.G. received grants from the Centre National d'Études Spatiales (CNES) at the French Alternative Energies and Atomic Energy Commission (CEA). R.A.G. also acknowledges funding from the European Community Seventh Framework Programme (FP7/2007–2013) under grants 312844 (SPACEINN) and 269194 (IRSES/ASK). This research was supported in part by the NSF under grant NSF PHY11-25915. Funding for the Stellar Astrophysics Centre is provided by The Danish National Research Foundation (grant agreement DNRF106). This research is supported by the ASTERISK project (ASTERoseismic Investigations with SONG and Kepler) funded by the European Research Council (grant agreement 267864). V.S.A. acknowledges support from VILLUM FONDEN (research grant 10118).

Author Contributions J.L.v.S. provided the physical interpretation of the rapid rotation and the rotational and stellar modelling. M.H.P. contributed to the design of the rotation tracer code, to ongoing YREC (Yale rotating stellar evolution code) development, and to interpretation of the results. T.S.M. carried out asteroseismic modelling portal (AMP) modelling of all targets. V.S.A. carried out Bayesian stellar algorithm (BASTA)–Garching stellar evolution code modelling. T.C., R.A.G. and S.M. developed and implemented the analysis of rotational modulation in Kepler data. G.R.D provided updated asteroseismic mode frequencies used in the modelling.

Author Information Reprints and permissions information is available at www.nature.com/reprints. The authors declare no competing financial interests. Readers are welcome to comment on the online version of the paper. Correspondence and requests for materials should be addressed to J.L.v.S. (jvansaders@obs.carnegiescience.edu) or R.A.G. (rafael.garcia@cea.fr) for computers code.

METHODS

Sample selection. Our sample can be divided into two principal target types: Kepler Asteroseismic Science Consortium (KASC) targets, and Kepler Objects of Interest (KOIs). We focus on those stars with (modelled) ZAMS $T_{\rm eff}$ values (defined as the point at which hydrogen fusion dominates the stellar luminosity) below 6,200 K, where magnetic braking should be most important. We show the positions of the selected stars on a Hertzsprung–Russell diagram in Extended Data Fig. 1, and period–age plot in Extended Data Fig. 2.

As described elsewhere[9], the asteroseismic sample is drawn from a magnitude-limited sample of 2,000 Sun-like stars that were selected for a one-month period of short-cadence (~1-minute) Kepler observations on the basis of their properties in the Kepler Input Catalog (KIC). Of these stars, roughly 500 displayed evidence of solar-like oscillations. A subset of targets with detections of oscillations that show high signal to noise ratio detections of oscillations were selected for continued monitoring over Kepler quarters 5–17. Of this sample, the mode frequencies for a subset of 61 high-signal-to-noise stars were extracted; there are high-resolution spectroscopic data for 46 of these. We modelled 42 of these 46 stars with the asteroseismic modelling portal (AMP, described below), excluding 4 targets whose spectra contained a complicated pattern of mixed modes. Of the 42 modelled targets, 11 were both detected in spot modulation and classified as 'simple' solar-like oscillators that did not show the seismic hallmarks of F-stars and evolved subgiants. A further three (non-overlapping) targets were added[7]. Of this sample of 14, 12 targets have AMP ZAMS $T_{\rm eff}$ values of less than 6,200 K, yielding a total of 12 stars in the KASC sample.

The KOI sample[9] was selected from the 77 KOIs observed in short cadence that displayed signatures of solar-like oscillations. Of these, 35 power spectra were of sufficient quality to extract individual mode frequencies to be modelled, 33 of which represent unevolved main-sequence stars. A subset of 11 have periods detected via spot modulation[6], 7 of which have an AMP ZAMS $T_{\rm eff}$ of less than 6,200 K.

Finally, we add the two well studied stars from the 16 Cygni binary to our sample; for these stars, asteroseismic ages[16] and rotation periods have been inferred from asteroseismic mode splittings[23]. In total, 21 stars are addressed in this analysis. Where available, we use the updated asteroseismic frequencies of ref. 24. Extended Data Table 1 shows the seismic (mass, age) and spectroscopic ($T_{\rm eff}$, [Fe/H]) values and rotation periods for these stars.

Age and period measurements. Asteroseismic ages are determined using two methodologies: AMP, which provides the ages used in most of this paper; and the Bayesian stellar algorithm (BASTA) pipeline, used to verify that the discrepancies in predicted and observed rotation periods are not the result of pipeline choice. AMP uses a genetic algorithm to perform a search for the global χ^2 minimum between the stellar observables and stellar model values[9]. The algorithm uses the Aarhus stellar evolution code (ASTEC) and adiabatic pulsation code (ADIPLS) to compute oscillation frequencies. The BASTA pipeline uses a Bayesian approach to model stars with a grid of models produced with the Garching stellar evolution code (GARSTEC). The input physics of the stellar models used in each method are detailed in refs 8–10.

Both methods use frequency spacings and spectroscopic constraints to identify the optimal stellar properties, but AMP also uses the individual frequencies by employing an empirical correction for surface effects. There are two main differences between the models used by BASTA and those used by AMP. BASTA–GARSTEC uses a fixed relationship between the initial helium and metallicity, anchored to zero metallicity at the primordial helium abundance and assuming $\Delta Y/\Delta Z = 1.4$ to reproduce the solar values (Y is the mass fraction of helium and Z is the mass fraction of all other elements excluding hydrogen and helium). It also uses a single solar-calibrated value of the mixing-length parameter for all models. AMP–ASTEC allows the initial helium to float independently of metallicity, and searches a wide range of values for the mixing-length parameter. Both sets of models include diffusion, although BASTA–GARSTEC includes both helium and heavy-metal diffusion, while AMP–ASTEC considers only helium diffusion.

We extract rotation periods using techniques[5] that we summarize briefly here (full period-extraction diagrams are available at http://irfu.cea.fr/Phocea/Vie_des_labos/Ast/ast_technique.php?id_ast=3607). For the corrected light curve of each Kepler star, the autocorrelation function (ACF) and a wavelets decomposition (period-time) are calculated. We collapse the wavelet decomposition on the period axis to obtain the global wavelet power spectrum (GWPS), and the peaks of this GWPS are fitted with gaussian functions. In parallel, we identify the peaks of the ACF. The derived surface rotation period is the result of the comparison of the ACF and GWPS analyses and is confirmed by a visual inspection of the light curves.

Stellar rotation models. We use a theoretical model grid[14] (using OPAL rather than OP opacities; all other inputs are unchanged), utilize the same loss-law calibration and form as in ref. 14, and assume solid-body rotation. The model grid is expanded to cover a wider range of metallicities and masses, namely $[Z/{\rm H}] = -0.4$ to $[Z/{\rm H}] = +0.4$, assuming a helium enrichment of $\Delta Y/\Delta Z = 1.0$ and no diffusion or gravitational settling. We use the 'fast launch' conditions[14] for modelling the rotation, but have validated that our results are insensitive to the choice of initial conditions. Changing the launch conditions typically shifts the period ratio (in sense of expected/observed) by less than 50% of the quoted errors, and shifts the fitted critical Rossby number to ${\rm Ro}_{\rm crit} = 2.15 \pm 0.08$. The model $\tau_{\rm cz}$ is the local convective overturn timescale, defined as the ratio of the typical mixing length to the convective velocity at one pressure scale height above the base of the convective envelope in the mixing length theory of convection. Under this definition, the solar rotation period ($P_\odot$) is 25.4 days, $\tau_{{\rm cz},\odot}$ is 1.015×10^6 s, and ${\rm Ro}_\odot = 2.16$.

The weakened magnetic braking is modelled by modifying the braking law such that a star with $P/\tau_{\rm cz} > {\rm Ro}_{\rm crit}$ is evolved under the assumption of conservation of angular momentum, such that the rotation period depends only on the changing moment of inertia of the star as it evolves. The modified loss law is given by the following equations (based on equations (1) and (2) in ref. 14):

$$\frac{{\rm d}J}{{\rm d}t} = \begin{cases} f_{\rm K} K_{\rm M} \omega \left(\dfrac{\omega_{\rm crit}}{\omega_\odot}\right)^2, & \omega_{\rm crit} \le \omega \dfrac{\tau_{\rm cz}}{\tau_\odot}, \quad {\rm Ro} \le {\rm Ro}_{\rm crit} \\ f_{\rm K} K_{\rm M} \omega \left(\dfrac{\omega \tau_{\rm cz}}{\omega_{\rm s} \tau_{{\rm cz},\odot}}\right)^2, & \omega_{\rm crit} > \omega \dfrac{\tau_{\rm cz}}{\tau_\odot}, \quad {\rm Ro} \le {\rm Ro}_{\rm crit} \\ 0, \quad {\rm Ro} > {\rm Ro}_{\rm crit} & \end{cases}$$

$$\frac{K_{\rm M}}{K_{{\rm M},\odot}} = c(\omega) \left(\frac{R}{R_\odot}\right)^{3.1} \left(\frac{M}{M_\odot}\right)^{-0.22} \left(\frac{L}{L_\odot}\right)^{0.56} \left(\frac{P_{\rm phot}}{P_{{\rm phot},\odot}}\right)^{0.44}$$

where $f_{\rm K}$ is a constant factor used to scale the loss law during the empirical fitting; $\omega_{\rm crit}$ is the saturation threshold (important only at young ages); $\tau_{\rm cz}$ is the convective overturn timescale; $P_{\rm phot}$ is the pressure at the photosphere; R is the radius; M is the mass; L is the luminosity; and $\odot$ refers to the Sun. The term $c(\omega)$ sets the centrifugal correction; because our stars are slowly rotating and the correction should be small, we set $c(\omega)$ to a constant value of 1. This braking law is fit to open-cluster data and the Sun, where the initial rotation period, disk-locking timescale, $\omega_{\rm crit}$, and $f_{\rm K}$ were allowed to vary, and all other parameters were determined using stellar evolutionary models[14]. When fitting for an optimal ${\rm Ro}_{\rm crit}$, we keep the parameters of the magnetic braking law calibrated on the Sun and open clusters fixed, and vary only the ${\rm Ro}_{\rm crit}$ at which braking is allowed to cease. ${\rm Ro}_{\rm crit}$ is optimized using a χ^2 figure of merit (valid under the assumption of independent observations and Gaussian uncertainties): $\chi^2 = \Sigma_i^N (P_{{\rm obs},i-{\rm mod},i})^2/(\sigma_{{\rm obs},i}^2 + \sigma_{{\rm mod},i}^2)$, where $\sigma_{{\rm obs},i}$ is the observational uncertainty on the extracted period, and $\sigma_{{\rm mod},i}$ represents the uncertainty on the model period given the uncertainties on the input masses, ages, and compositions. We derive uncertainties on ${\rm Ro}_{\rm crit}$ using bootstrap resampling, drawing a 21-star sample with replacement from the original data 50,000 times, and recalculating the best-fit ${\rm Ro}_{\rm crit}$ for each realization. Cluster data and the Sun are not used in this fit. An alternate fit allowing parameters important for late-time braking to vary ($f_{\rm K}$, ${\rm Ro}_{\rm crit}$) and including intermediate-age and older rotation data from the seismic sample, NGC 6819, and the Sun (52 stars in total) yields a best-fit ${\rm Ro}_{\rm crit}$ of 2.1 ± 0.1, with $f_{\rm K} = 8.4 \pm 0.2$.

Predicted model periods are obtained by using the mass and age from the asteroseismic pipelines coupled with the spectroscopic metallicity[8–10,16]. Model uncertainties are estimated by generating 50,000 (20,000 for ${\rm Ro}_{\rm crit} + f_K$ fit) realizations of the input parameters (M, t and [Fe/H]), where values are drawn from a Gaussian distribution centred on the observed value, with 1σ errors defined by the observational uncertainties. While we search in the fundamental space of mass, age and composition, we select only models which fall within 5σ of the observed $T_{\rm eff}$. This constraint has little or no effect for unevolved stars, but ensures that stars at the turnoff (KIC 6196457 and KIC 8349582 in particular) are not assigned artificially long rotation periods due to mass–age combinations that fall on the subgiant branch. 1σ uncertainties on the model periods are defined as the values that enclose 68% of the resulting models.

Empirical gyrochronology relations. We verify that the unexpectedly rapid rotation in old, solar-like stars is independent of the spin-down prescription by repeating our exercise with an empirical literature gyrochronology relation[2]. We replicate Fig. 2 in Extended Data Fig. 3 with predicted periods drawn from an empirical gyrochronology calibration, based on equation (32) in ref. 2:

$$t = \frac{\tau}{k_{\rm C}} \ln\left(\frac{P}{P_0}\right) + \frac{k_{\rm I}}{2\tau}(P^2 - P_0^2)$$

where t is the age, τ is the convective overturn timescale, P is the period, and P_0 is the initial period. We adopt values for k_C of 0.646 million years (Myr) per day and for $k_{\rm I}$ of 452 days per Myr; $P_0 = 1.1$ days, and the global $\tau - T_{\rm eff}$ relation is as used in refs 2,4. 50,000 realizations of the combination ($T_{\rm eff}$, t) are drawn from a Gaussian distribution centred on the measured values, with a 1σ width defined by the quoted observational errors on the central values. These empirical relationships do not account for the physical expansion of stars as they evolve (particularly near the end of the main sequence) and therefore tend to predict somewhat more rapid rotation than do full theoretical models near the main sequence turnoff.

Cluster data. To provide comparison with the typical gyrochronological calibrators, we draw cluster data from a variety of literature sources. For the cluster M37 we adopt the following cluster parameters[15]: extinction, $E(\mathrm{B-V}) = 0.227 \pm 0.038$ mag; total metal abundance $[\mathrm{M/H}] = 0.045 \pm 0.044$ dex; age = 550 ± 30 Myr. Rotation data and cluster parameters[25] for Praesepe (M44) are included, with $E(\mathrm{B-V}) = 0.027 \pm 0.004$, $[\mathrm{Fe/H}] = 0.11 \pm 0.03$, and $\log(\mathrm{age}) = 8.77 \pm 0.1$. For NGC 6811, we adopt the *g-r* colours, $E(\mathrm{B-V})$ value of 0.1, and rotation periods as in ref. 26, as well as the [M/H] value of -0.1 ± 0.01 and age of 1.00 ± 0.05 Gyr from ref. 27. Finally, for NGC 6819 we use the rotation periods and $B-V$ colours from ref. 4, with the age (2.5 ± 0.2 Gyr) and adopted metallicity (0.09 ± 0.03) from ref. 28. $B-V$ colours are converted into temperatures and stellar masses using Yale rotating stellar evolution (YREC) isochrones[29]. We model cluster stars in the same manner as the seismic targets, with 10,000 mass–age–composition realizations for each star. We display the mean cluster rotation periods for all stars within the ZAMS T_{eff} bins, with errors representing the 16th and 84th percentiles. In M37 and Praesepe in particular, the rotational distribution displays a range resulting from spread in the initial rotation periods.

Sample biases. We demonstrate that our results are unlikely to be a consequence of selection bias in our sample. The sample is subject to two sources of selection bias: asteroseismic detectability, and the detectability of spot modulation.

Detailed asteroseismic analysis requires a high signal-to-noise detection of the power excess from oscillations. Oscillation amplitudes scale roughly as $A_{\max} \propto (L/M)\,(T_{\mathrm{eff}})^{-2}$ (equation (7) from ref. 30, referring to $l = 0$ radial modes); seismic samples are therefore strongly biased towards more-massive stars. There is also a bias towards bright targets, where lower noise levels contribute to detectability. Our sample is drawn from two subsets of stars: the one-month survey stars from the seismic sample, and the KOIs. We expect the one-month survey seismic detections at magnitudes of K_{p} of less than ~10, while the roughly 1,000-day time series in short cadence collected for the KOI sample allow detections out to $K_{\mathrm{p}} \approx 12$, which well describes the actual magnitude distribution of our sample (see Fig. 6 in ref. 30). The strong trends with magnitude and mass are well predicted by basic scaling arguments, save for the dependence on activity: active stars are less likely to be detected in oscillations[30]. Our sample is selected seismically, and we do not expect the well understood seismic biases to favour rapid rotators (apart from the obvious mass dependence).

Variability owing to starspots scales with the rotation period, in the sense that more rapid rotation is associated with higher amplitudes of variability[15]. One could imagine that we are detecting the rapidly rotating tail of a distribution of rotation periods, or detecting objects spun up by binary/planetary interactions or mergers.

This first case is at odds with what we know from open clusters: as late as 2.5 Gyr, there is a converged, well defined rotational sequence that shows very little scatter at fixed mass[4]. If we are in fact detecting a rapidly rotating subset of the population, the dispersion in rotation and spin-down rates must set in after several billion years, or it would be visible in the open-cluster data. If there is dispersion in the rotation periods, it represents a serious challenge to the validity of gyrochronology for old stars, regardless of its source.

The pipeline used to extract the rotation periods for this work has been tested with an injection and recovery exercise[17]. Our recovery fraction is shown in Extended Data Fig. 4, and demonstrates that we should be able to detect stars that are substantially less active than the Sun at longer periods. However, this exercise does not account for stars that simply cease to have spots to detect on their surfaces; under this scenario, slow rotators could exist but be undetectable. We cannot directly combat this concern given our current data set, although we can examine the case of 16 Cygni (16 Cyg). 16 Cyg A and B are not detected in spot modulation; their periods are derived from asteroseismic frequency splittings, which yield periods that probe the envelope rotation[23]. If we assume that these stars have solar-like rotation profiles, then the seismic rotation periods are directly comparable to the surface periods. This pair displays the same anomalously rapid rotation as objects detected in spot modulation, providing evidence against the argument that stars undetected in spot modulation are simply more slowly rotating. It is also worth noting that our own Sun would be undetectable during the minimum of its activity cycle (see ref. 17). Our non-detections could equally be the result of the normal variations in the activity of Sun-like stars, rather than a period bias.

Finally, we examine the possibility of interactions or mergers with other bodies. In our sample, 16 Cyg A and B, and KIC 3427720 and KIC 9139151, are known or suspected binaries[5]. In each case, the components are well separated, and the binary orbits are estimated well in excess of 10,000 years. In order for a companion to affect rotation considerably, it must be at orbital periods comparable to the rotation period, and will therefore be unresolved. The KOI sample has undergone the extensive vetting that is associated with planet detection; all planets are confirmed, and there is no evidence of transit timing variations that would accompany a close stellar companion. System stability is unlikely for binary orbits of the order of 30 days that contain even a low-mass stellar companion[31]. Likewise, there is no evidence for interaction between the planets and the host stars in the KOI sample[6], and no known hot Jupiters. In the case of the seismic sample, there is no evidence for double-lined binaries, photometric–spectroscopic temperature disagreements, multiple oscillating components, or unusual dilution of the seismic power spectra, and no evidence of eclipses. Finally, if mergers (planetary or stellar) were responsible for all detections of rapid rotation, then the 50% detection rate of the 'simple stars'[7] in spot modulation implies an uncomfortably high merger rate.

The asteroseismic age scale. We carry out two tests to demonstrate that the discrepancy between the expected and observed rotation periods is not due to a systematic bias in the ages with roots in the asteroseismic age scale. We show that ages derived with the BASTA pipeline display the same trend in rotation period, and that systematically shifting the asteroseismic ages, while improving the fit, is inferior to instituting a Rossby threshold.

Extended Data Fig. 5 provides period ratio plots using the BASTA ages and BASTA ZAMS T_{eff} determinations. The systematic trend in the period ratios survives. The Barnes relation[2] fits with $\chi^2 = 184.3$, and the fiducial models[14] with $\chi^2 = 68.4$. A fit for $\mathrm{Ro_{crit}}$ using the BASTA ages yields $\mathrm{Ro_{crit}} = 2.67 \pm 0.50$. Bootstrap resampling demonstrates that this number is sensitive to whether KIC 8349582 is drawn; if KIC 8349582 is excluded, the fit becomes $\mathrm{Ro_{crit}} = 2.12 \pm 0.12$.

We also investigate the possibility that the seismic age scale is systematically shifted relative to the true ages. We perform model fits with the fiducial braking law with an extra parameter that allows for a systematic age shift. For the AMP ages, χ^2 is minimized with the Barnes relation with a systematic shift of 35% and a χ^2 of 78.5. Likewise, the fiducial models[14] prefer a shift of 20 ± 3% with a χ^2 of 26.9. In both cases, the required systematic shifts are larger than the estimated 9.6% systematic uncertainties in seismic ages[10].

Finally, to verify that we are not biased by the fact that the ages and periods were determined using different evolution codes, we tune the physics in the fiducial models[14] to match that of the AMP models, and predict the rotation periods for the central AMP values of the masses, ages, and compositions of each star. In particular, we match the diffusion physics, opacity tables, equation of state, helium and metal abundances, boundary conditions, and important nuclear reaction rates present in the ASTEC code used for AMP. The results are presented in Extended Data Fig. 6, and demonstrate that the discrepancy between the predicted and observed periods is preserved. We conclude that our result is not the consequence of assumptions about the stellar physics included in models.

Code availability. The AMP science code used to infer stellar ages can be downloaded at https://amp.phys.au.dk/about/evolpack. Code for the period extraction and rotational evolution will be publicly released upon completion of the necessary documentation. YREC likewise has no public documentation, and has not been publicly released. BASTA is undergoing major revisions for increased speed and is not yet publicly available.

23. Davies, G. R. *et al.* Asteroseismic inference on rotation, gyrochronology and planetary dynamics of 16 Cygni. *Mon. Not. R. Astron. Soc.* **446,** 2959–2966 (2015).
24. Davies, G. R. *et al.* Oscillation frequencies for 35 Kepler solar-type planet-hosting stars using Bayesian techniques and machine learning. Preprint at http://arXiv.org/abs/1511.02105 (2015).
25. Kovacs, G. *et al.* Stellar rotational periods in the planet hosting open cluster Praesepe. *Mon. Not. R. Astron. Soc.* **442,** 2081–2093 (2014).
26. Meibom, S. *et al.* The *Kepler* cluster study: stellar rotation in NGC6811. *Astrophys. J.* **733,** L9–L14 (2011).
27. Yontan, T. CCD UBVRI photometry of NGC 6811. *Astrophys. Space Sci.* **355,** 267–281 (2015).
28. Jeffries, M. W. WOCS 40007: a detached eclipsing binary near the turnoff of the open cluster NGC 6819. *Astron. J.* **146,** 58–78 (2013).
29. An, D. *et al.* The distances to open clusters from main-sequence fitting. III. Improved accuracy with empirically calibrated isochrones. *Astron. J.* **655,** 233–260 (2007).
30. Chaplin, W. J. *et al.* Predicting the detectability of oscillations in solar-type stars observed by *Kepler*. *Astrophys. J.* **732,** 54–62 (2011).
31. Holman, M. J. & Weigert, P. A. Long-term stability of planets in binary systems. *Astron. J.* **117,** 621–628 (1999).

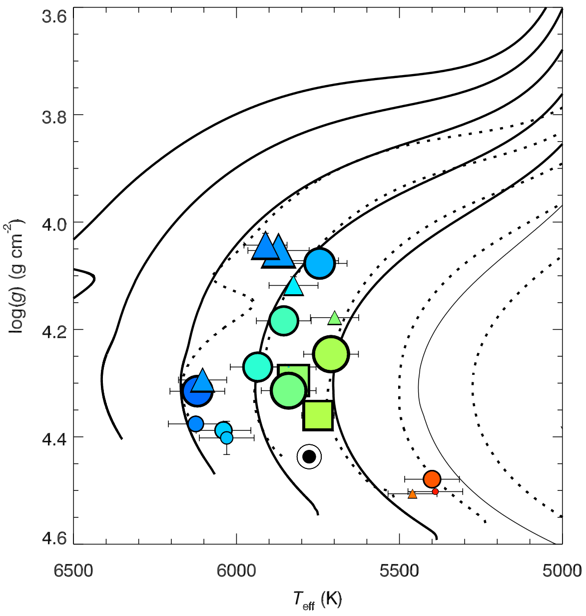

Extended Data Figure 1 | The positions of all 21 Kepler stars on the Hertzsprung–Russell diagram. We plot spectroscopic T_{eff} (a proxy for mass) versus seismic log(g) (surface gravity), with 1σ observational error bars; the symbol size is proportional to the period ratio (AMP ages, fiducial models[14]). Colours and symbol conventions are as in Fig. 2. Evolutionary tracks are overplotted for [Z/H] = +0.3 (dotted lines) and [Z/H] = −0.1 (solid lines), for masses 0.8–1.3 $M_{\odot}$ in increments of 0.1 $M_{\odot}$. ([Z/H] = +0.3, M = 0.8 $M_{\odot}$ is beyond the plotted area.)

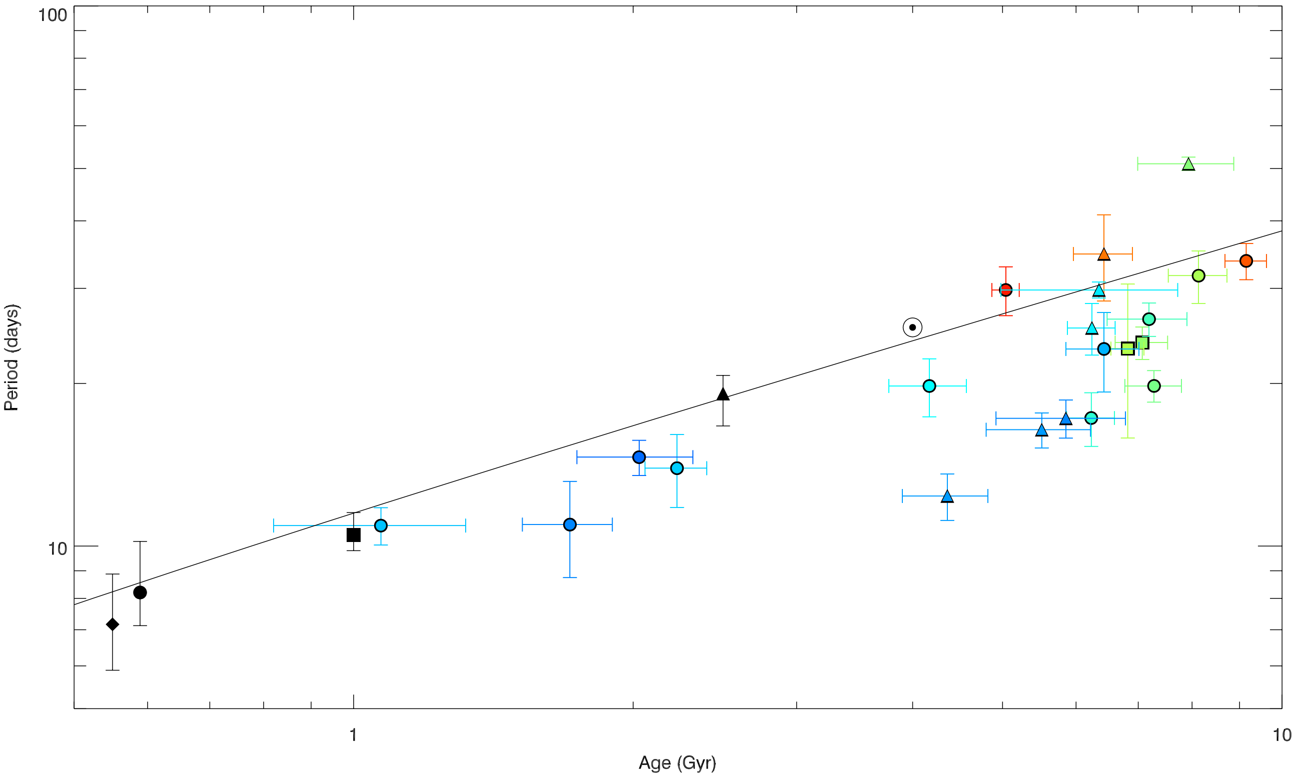

Extended Data Figure 2 | Period–age plot of sample stars. The 21-star sample, with observed rotational periods plotted against AMP asteroseismic ages. Symbol conventions are as in Fig. 2. The solid line denotes the empirical relation[2] for $T_{eff} = 5{,}800$ K (approximately equal to the mean sample T_{eff}). All error bars represent 1σ.

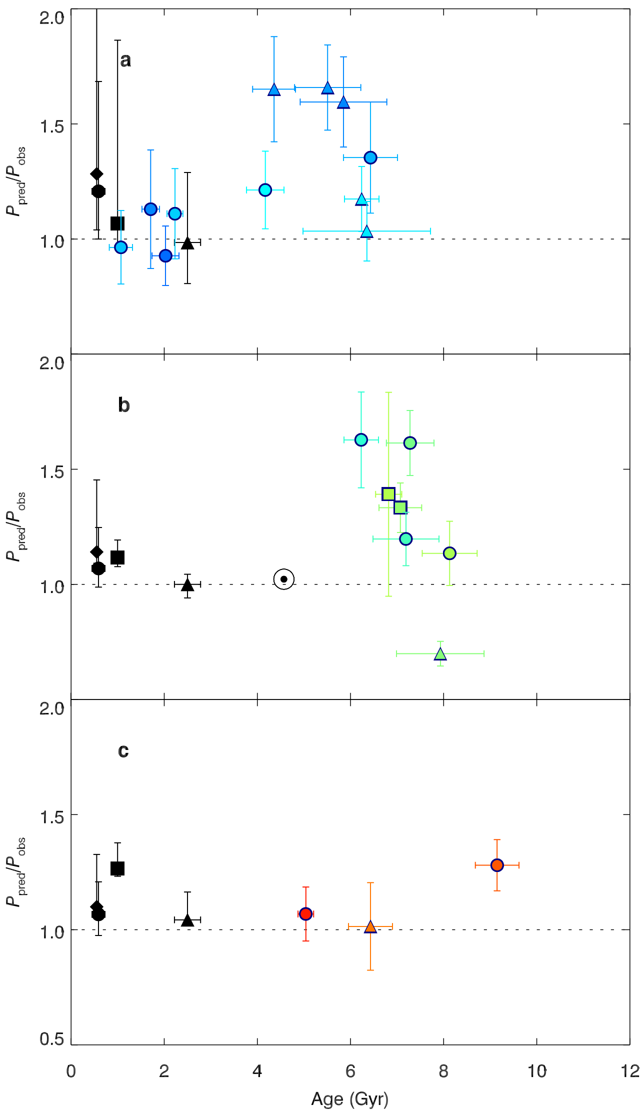

Extended Data Figure 3 | Period ratios using empirical gyrochronology relations. Ratios of predicted periods[2] to observed periods are plotted as a function of the AMP asteroseismic age, and divided according to AMP ZAMS T_{eff} (**a**, ZAMS T_{eff} = 5,900–6,200 K; **b**, ZAMS T_{eff} = 5,600–5,900 K; **c**, ZAMS T_{eff} = 5,100–5,400 K.) Error bars represent 1σ. Symbol conventions are as in Fig. 2.

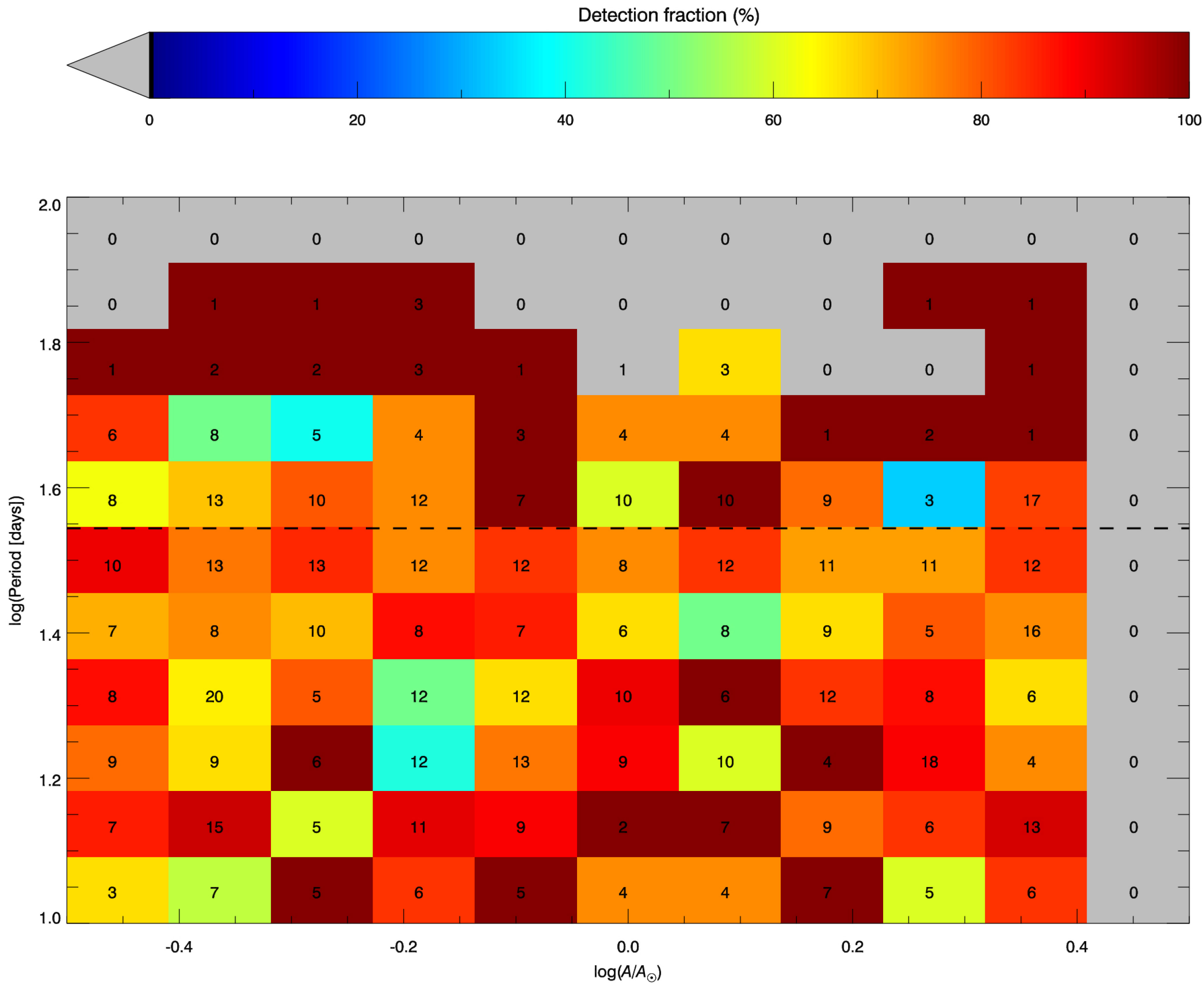

Extended Data Figure 4 | Detectability of stars in spot modulation. Detection fractions for the 750 stars with noise in the hound-and-hare exercise of ref. 17, as a function of activity level A (where the activity level of the Sun is defined as $A_{\odot} = 1$) and rotation period. The total number of light curves searched for periodicity in each cell is overplotted. The dashed black line at $P = 35$ days represents the expected period for stars like the Sun under traditional gyrochronology relations found in the literature.

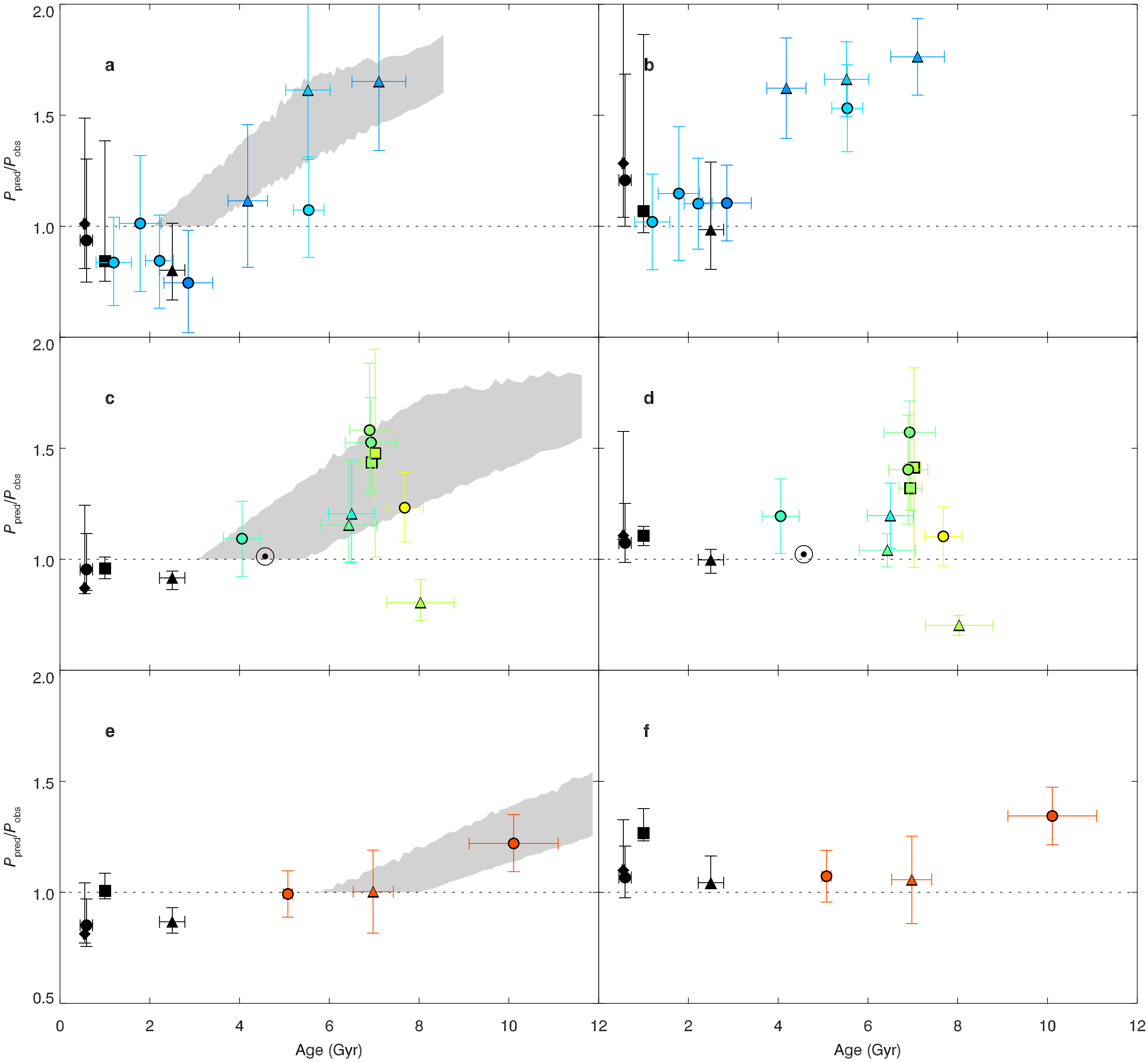

Extended Data Figure 5 | Predicted versus observed rotation periods using ages determined with BASTA. a, **c**, **e**, Plotted are the ratios of the periods predicted using the fiducial models[14] to the observed rotation periods, as a function of stellar age. The grey band represents the offset expected from models in which $Ro_{crit} = 2.16$. All error bars represent 1σ. **b**, **d**, **f**, Ratios of the predicted periods obtained from the empirical relation[2] to the observed periods, plotted against stellar age. Stars are divided according to ZAMS T_{eff}, using BASTA ZAMS T_{eff} values: **a**, **b**, 5,900–6,200 K; **c**, **d**, 5,500–5,900 K; **e**, **f**, 5,100–5,400 K. All symbol conventions are as in Fig. 2.

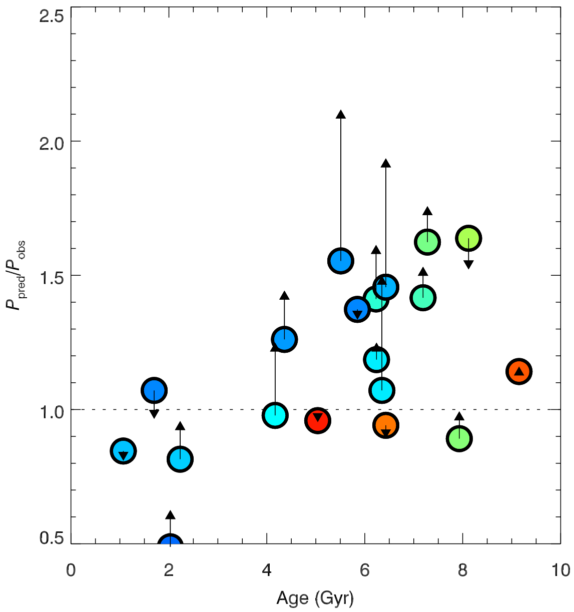

Extended Data Figure 6 | The shift in the period ratios induced by changing the stellar model input physics. Circles are colour-coded according to ZAMS T_{eff} as in Fig. 2. Ratios of the periodicity expected from the fiducial model[14] to the observed periodicity are plotted against age. Arrows denote the shift in the period ratio that occurs when YREC models[14] are run to match the AMP–ASTEC physics.

Extended Data Table 1 | Rotation periods, asteroseismic data and spectroscopic quantities for sample stars

KIC	AMP Mass	AMP Age	AMP log(g)	AMP ZAMS T_{eff}	BASTA/GARSTEC Mass	BASTA/GARSTEC Age	BASTA/GARSTEC ZAMS T_{eff}	Spectroscopic T_{eff}	Spectroscopic [Fe/H]	Period	Note
16Cyg A	1.10±0.02	7.07±0.46	4.295	5677	1.04±0.01	6.95±0.26	5668	5825±50	+0.09±0.02	23.8±1.7	seismic period
16Cyg B	1.06±0.02	6.82±0.28	4.360	5629	0.998±0.005	7.02±0.14	5592	5750±50	+0.05±0.02	23.2±7.4	seismic period
3427720	1.13±0.04	2.23±0.17	4.388	5985	1.12±0.02	2.22±0.31	6019	6040±84	-0.03±0.09	13.9±2.1	seismic
3656476	1.17±0.03	8.13±0.59	4.246	5642	1.07±0.01	7.68±0.42	5525	5710±84	+0.25±0.09	31.7±3.5	seismic
5184732	1.27±0.04	4.17±0.40	4.270	5905	1.18±0.02	4.05±0.42	5810	5840±84	+0.38±0.09	19.8±2.4	seismic
6116048	1.01±0.03	6.23±0.37	4.270	5838	1.06±0.02	5.54±0.34	5943	5935±84	-0.24±0.09	17.3±2.0	seismic
6196457	1.23±0.04	5.51±0.71	4.053	6064	1.21±0.02	5.52±0.50	5991	5871±94	+0.17±0.11	16.4±1.2	KOI
6521045	1.04±0.02	6.24±0.37	4.118	5933	1.11±0.02	6.50±0.51	5886	5825±75	+0.02±0.10	25.3±2.8	KOI
7680114	1.13±0.03	7.19±0.70	4.184	5801	-- --	-- --	-- --	5855±84	+0.11±0.09	26.3±1.9	seismic
7871531	0.84±0.02	9.15±0.47	4.479	5253	0.84±0.02	10.10±0.99	5240	5400±84	-0.24±0.09	33.7±2.6	seismic
8006161	1.04±0.02	5.04±0.17	4.502	5165	0.948±0.005	5.08±0.10	5250	5390±84	+0.34±0.09	29.8±3.1	seismic
8349582	1.19±0.04	7.93±0.94	4.178	5695	1.07±0.02	8.03±0.75	5630	5699±74	+0.30±0.10	51.0±1.5	KOI
9098294	1.00±0.03	7.28±0.51	4.314	5718	1.01±0.02	6.93±0.57	5734	5840±84	-0.13±0.09	19.8±1.3	seismic
9139151	1.14±0.03	1.71±0.19	4.376	6092	1.16±0.02	1.79±0.46	6019	6125±84	+0.11±0.09	11.0±2.2	seismic
9955598	0.96±0.01	6.43±0.47	4.506	5307	0.89±0.01	6.98±0.45	5250	5460±75	+0.08±0.10	34.7±6.3	KOI
10454113	1.19±0.04	2.03±0.29	4.315	6138	1.15±0.03	2.86±0.54	6095	6120±84	-0.06±0.09	14.6±1.1	seismic
10586004	1.16±0.05	6.35±1.37	4.072	5943	1.18±0.03	6.43±0.62	5753	5770±83	+0.29±0.10	29.8±1.0	KOI
10644253	1.13±0.05	1.07±0.25	4.402	6001	1.16±0.02	1.20±0.39	5991	6030±84	+0.12±0.09	10.91±0.87	seismic
10963065	1.07±0.02	4.36±0.46	4.294	6063	1.09±0.02	4.18±0.44	6076	6104±74	-0.20±0.10	12.4±1.2	KOI
11244118	1.10±0.05	6.43±0.58	4.077	6023	1.13±0.02	6.90±0.44	5677	5745±84	+0.35±0.09	23.2±3.9	seismic
11401755	1.03±0.05	5.85±0.93	4.043	6094	1.06±0.03	7.10±0.60	6057	5911±66	-0.20±0.06	17.2±1.4	KOI

Units are as follows: mass, solar masses; age, Gyr; log(g), g cm^{-2}, T_{eff}, K; period, days. Quoted errors are given to 1σ.